

Diffraction satellites in indium caused by thermal-diffuse scattering

A. S. Bakulin

Department of Chemistry, Purdue University, West Lafayette, Indiana 47907

G. Lacueva

Physics Department, John Carroll University, University Heights, Ohio 44118

A. W. Overhauser

Department of Physics, Purdue University, West Lafayette, Indiana 47907

(Received 10 December 1998)

An x-ray search for charge-density-wave structure in indium revealed more than one hundred diffraction peaks having half integral (h,k,l) . However, the ‘‘satellite’’ intensities were found to be proportional to temperature (above 20 K), which proves they are caused by thermal-diffuse scattering (TDS) involving phonons near the $\{\frac{1}{2}, \frac{1}{2}, \frac{1}{2}\}$ points of the Brillouin-zone boundary. Theoretical TDS peaks, which were calculated for forty half-integral $\{h,k,l\}$ families, explain the observed intensities. The peaks arise from a sharp dip in the slow shear phonon mode near $\{\frac{1}{2}, \frac{1}{2}, \frac{1}{2}\}$ for q -space trajectories nearly parallel to the hexagonal face of the relevant extended zone boundary. (TDS peaks do not appear in scans along trajectories that are nearly perpendicular to the hexagonal face of an extended zone boundary.) The dynamic pseudopotential model for lattice vibrations in metals was employed. [S0163-1829(99)03919-3]

I. INTRODUCTION

Indium would be face-centered cubic were it not for a 7.5% tetragonal extension along one of its (otherwise) cubic axes. The cause of this distortion is unknown. What has also remained a puzzle for more than 40 years is the behavior of the c -axis lattice parameter versus temperature, shown in Fig. 1 together with the (ordinary) expansion of the a -axis parameter with increasing T . The data are from Graham, Moore, and Raynor.¹ Not only is the c -axis expansion coefficient too small by an order of magnitude, it becomes negative for $T > 275$ K.

Another unexpected property of In is the reduction in the Debye, AT^3 , component of the specific heat in the superconducting state (relative to its magnitude in the normal state). The anticipated fractional reduction is expected to be $\sim 10^{-5}$, a typical value observed in several superconductors² by precision acoustic measurements. However, the reduction for In is $\sim 10\%$, too large by four orders of magnitude,³ even after allowance for nuclear hyperfine effects.⁴ This discrepancy has never been explained.

The motivation for the x-ray diffraction study described below stems from a realization that a charge-density-wave (CDW) broken symmetry could possibly explain the phenomena just mentioned. If a CDW has wave vector \mathbf{Q} , then conduction electron momentum states $\{\mathbf{k}\}$ will become mixed with $\{\mathbf{k} \pm \mathbf{Q}\}$ components.⁵ If the angle between \mathbf{Q} and the c axis is small enough, i.e., less than 55° , the kinetic pressure of the admixed momentum components will lead to a lattice expansion along the c axis. (We assume that there would be a family of four or eight $\{\mathbf{Q}\}$ so that tetragonal symmetry would occur.) We anticipate that the amplitude p of each CDW would be related to the tetragonal distortion

$$p^2 \approx \mu \left(\frac{c}{a} - 1 \right), \quad (1)$$

where μ is a constant. Now it has been pointed out that the temperature dependence of $p(T)$ for a spin-density wave or a CDW is similar to that for a superconducting energy gap.⁶ Accordingly, the strange behavior of $c(T)$, shown in Fig. 1, can be interpreted as a consequence of the decrease in CDW amplitude with increasing T . By comparing the behavior of $(c/a - 1)$ with $\Delta^2(T)$ for a superconducting energy gap,⁷ we surmise that In would become cubic ($c/a = 1$) near 650 K. Unfortunately, In melts at 430 K, so this estimate cannot be checked.

A CDW structure leads to low-frequency phason modes,⁸ and these are heavily damped.⁹ Phason spectral density will then contribute to the AT^3 term in the specific heat.¹⁰ Most of this contribution will disappear when phason damping is suppressed by the presence of a superconducting energy gap 2Δ at the Fermi surface. Accordingly, the (unexpected) drop in the AT^3 specific heat might thereby be explained. The possibility of understanding for the first time both of these long-standing anomalies, described above, led us to search for CDW x-ray diffraction satellites.

II. X-RAY DIFFRACTION SEARCH FOR CDW SATELLITES

A search for CDW satellites in In is simplified by the requirement that the CDW $\{\mathbf{Q}_i\}$ must be commensurate with the lattice. In fact the $\{h_i, k_i, l_i\}$ must be integral or half integral. This condition derives from the observed sharpness of the nuclear quadrupole resonance.^{11,12} (Otherwise, hyperfine electric-field gradients would depend on the nuclear site.) Also, $|\mathbf{Q}_i|$ should nearly equal the diameter, $2k_F = 3.01 \text{ \AA}^{-1}$, of the conduction-electron Fermi sphere.⁶ Both conditions are satisfied if the CDW structure is a family of eight $\{\mathbf{Q}_i\}$

$$\left\{ \pm \frac{3}{2}, \pm \frac{1}{2}, \frac{3}{2} \right\} \quad \text{and} \quad \left\{ \pm \frac{1}{2}, \pm \frac{3}{2}, \frac{3}{2} \right\}, \quad (2)$$

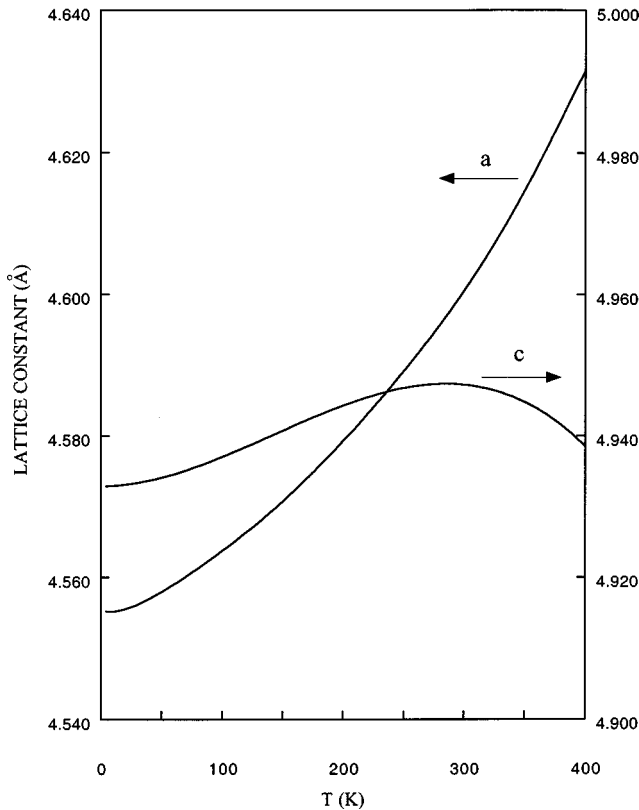


FIG. 1. Temperature dependence of the lattice constants a and c for (tetragonal) indium. ($c/a=1.075$ at room temperature.)

expressed in reciprocal lattice units ($2\pi/a, 2\pi/a, 2\pi/c$). Alternatively, a family of four CDW's

$$\left\{ \pm \frac{3}{2}, \pm \frac{3}{2}, \frac{1}{2} \right\}, \quad (3)$$

would also satisfy both conditions. However, these latter $\{\mathbf{Q}_i\}$ have a 77° angle with the c axis, and would likely lead instead to $c/a < 1$. The angle of the $\{\mathbf{Q}_i\}$ family (2) is 47° , which is smaller than 55° , the limiting value separating tetragonal extension from contraction.

We employed a NONIUS-ENRAF CAD4 four-circle diffractometer to scan 512 half-integral (hkl) points. Since the In single crystal was a disc, 11 mm in diameter and 4-mm thick, the incident or diffracted beam was blocked more often than not. The axis of the cylindrical crystal was approximately $[212]$. Nevertheless, we found 118 satellitelike diffraction peaks. Mo $K\alpha$ radiation ($\lambda = 0.71 \text{ \AA}$) was used with a graphite monochromator on the incident beam. The anode voltage was set at 30 kV, so there was no $\frac{1}{2}\lambda$ component in the beam. (A 0.355 \AA photon cannot be created by a 30 keV electron.) That there was indeed no second-order contamination was proved by the absence of a peak at (100) and other integral, non-Bragg points. (Such reflections did appear if the anode voltage was set to 40 kV.) The anode current was 20 ma; each $\theta-2\theta$ scan lasted 10 min. The diffraction feature at $(\frac{5}{2}, \frac{3}{2}, \frac{1}{2})$ is shown in Fig. 2. All half-integral peaks had a comparable width. Also shown is the (202) Bragg peak after reduction by a factor 2000. The width of this peak indicates the instrumental resolution and sample quality. Table I lists all forty "satellite" families that were studied. The relative integrated intensities observed for each family are shown in

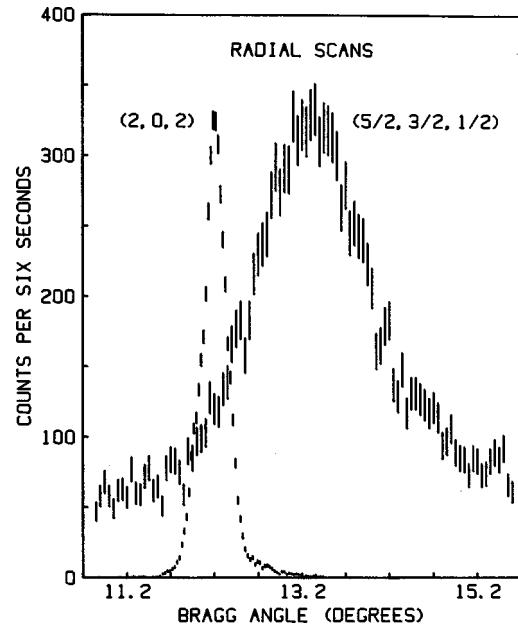


FIG. 2. Radial ($\theta-2\theta$) scan at room temperature through the $(\frac{5}{2}, \frac{3}{2}, \frac{1}{2})$ point in the reciprocal space of In. Mo $K\alpha$ x-rays ($\lambda = 0.71 \text{ \AA}$) were employed. The (202) Bragg reflection, reduced by a factor 2000, is shown for comparison.

the first column, and were normalized to unity for the $(\frac{5}{2}, \frac{3}{2}, \frac{1}{2})$ family. (The intensity of the strongest reflection from each family was, of course, the value chosen.)

The intensity of a CDW satellite should decrease with increasing T ; so such anticipated behavior must be verified. Since a low-temperature cryostat was not available for the CAD4 diffractometer, the temperature dependence of the half-integral superstructure was investigated at the National Synchrotron Light Source. Beam line X-18A was employed with $\lambda = 1.38 \text{ \AA}$. A double-crystal Si (111) monochromator was used with a focusing, specular-reflection toroidal mirror. (We checked that there was no $\frac{1}{2}\lambda$ component.) We found that the half-integral "satellite" intensities were approximately proportional to T between 20 and 200 K. Synchrotron data for the $(\frac{5}{2}, \frac{3}{2}, \frac{1}{2})$ peak are shown in Fig. 3. Consequently, the "satellites" are caused by thermal-diffuse scattering (TDS) of phonons near the $\{\frac{1}{2}, \frac{1}{2}, \frac{1}{2}\}$ points of the Brillouin-zone boundary; and not by CDW diffraction.

III. PHONON SPECTRUM OF INDIUM

The interesting question that presents itself is how phonon TDS can give rise to relatively sharp "satellite" structure, exemplified in Fig. 2 and observed for 23 of the 40 families listed in Table I. TDS peaks are always present at Bragg reflections, and result from scattering by small- q acoustic phonons (since $\omega_j \rightarrow 0$ as $q \rightarrow 0$). The TDS peaks discovered here must arise from phonons having \mathbf{q} near the centers of the hexagonal faces of the Brillouin-zone boundaries. A peak can be caused by a sharp dip in $\omega_j(\mathbf{q})$ or, alternatively, by rapid variation of the phonon polarization vector with \mathbf{q} .

The phonon spectrum of In has been measured by Smith and Reichardt.¹³ A theoretical fit to the data using the dynamic pseudopotential model¹⁴ has been made by Chen,

TABLE I. Relative intensities of "satellite"-like diffraction peaks in indium caused by TDS for 40 half-integral (h,k,l) families. (Each family has 16 equivalent scattering vectors, but only 8 if $h = k$.) The intensities have been normalized to unity for the $(\frac{5}{2}, \frac{3}{2}, \frac{1}{2})$ family.

| Family | Experimental | Theoretical |
|--|--------------|-------------|
| $\begin{Bmatrix} 1 & 1 & 1 \\ 2 & 2 & 2 \end{Bmatrix}$ | 0 | 0 |
| $\begin{Bmatrix} 1 & 1 & 3 \\ 2 & 2 & 2 \end{Bmatrix}$ | 0 | 0 |
| $\begin{Bmatrix} 3 & 1 & 1 \\ 2 & 2 & 2 \end{Bmatrix}$ | 0.2 | 0.2 |
| $\begin{Bmatrix} 3 & 1 & 3 \\ 2 & 2 & 2 \end{Bmatrix}$ | 0.3 | 0.2 |
| $\begin{Bmatrix} 3 & 3 & 1 \\ 2 & 2 & 2 \end{Bmatrix}$ | 0 | 0 |
| $\begin{Bmatrix} 1 & 1 & 5 \\ 2 & 2 & 2 \end{Bmatrix}$ | 0 | 0 |
| $\begin{Bmatrix} 3 & 3 & 3 \\ 2 & 2 & 2 \end{Bmatrix}$ | 0 | 0 |
| $\begin{Bmatrix} 5 & 1 & 1 \\ 2 & 2 & 2 \end{Bmatrix}$ | 0.2 | 0.2 |
| $\begin{Bmatrix} 3 & 1 & 5 \\ 2 & 2 & 2 \end{Bmatrix}$ | 0.6 | 0.4 |
| $\begin{Bmatrix} 5 & 1 & 3 \\ 2 & 2 & 2 \end{Bmatrix}$ | 0.5 | 0.4 |
| $\begin{Bmatrix} 5 & 3 & 1 \\ 2 & 2 & 2 \end{Bmatrix}$ | 1.0 | 1.0 |
| $\begin{Bmatrix} 3 & 3 & 5 \\ 2 & 2 & 2 \end{Bmatrix}$ | 0.5 | 0.3 |
| $\begin{Bmatrix} 5 & 3 & 3 \\ 2 & 2 & 2 \end{Bmatrix}$ | 1.0 | 1.0 |
| $\begin{Bmatrix} 1 & 1 & 7 \\ 2 & 2 & 2 \end{Bmatrix}$ | 0.4 | 0.3 |
| $\begin{Bmatrix} 5 & 1 & 5 \\ 2 & 2 & 2 \end{Bmatrix}$ | 0 | 0 |
| $\begin{Bmatrix} 7 & 1 & 1 \\ 2 & 2 & 2 \end{Bmatrix}$ | 0.9 | 0.8 |
| $\begin{Bmatrix} 5 & 5 & 1 \\ 2 & 2 & 2 \end{Bmatrix}$ | 0 | 0 |
| $\begin{Bmatrix} 3 & 1 & 7 \\ 2 & 2 & 2 \end{Bmatrix}$ | 0.2 | 0.2 |
| $\begin{Bmatrix} 5 & 3 & 5 \\ 2 & 2 & 2 \end{Bmatrix}$ | 0.6 | 0.7 |
| $\begin{Bmatrix} 7 & 1 & 3 \\ 2 & 2 & 2 \end{Bmatrix}$ | 0.6 | 0.6 |
| $\begin{Bmatrix} 5 & 5 & 3 \\ 2 & 2 & 2 \end{Bmatrix}$ | 0 | 0 |
| $\begin{Bmatrix} 7 & 3 & 1 \\ 2 & 2 & 2 \end{Bmatrix}$ | 0.2 | 0.2 |
| $\begin{Bmatrix} 3 & 3 & 7 \\ 2 & 2 & 2 \end{Bmatrix}$ | 0 | 0 |
| $\begin{Bmatrix} 7 & 3 & 3 \\ 2 & 2 & 2 \end{Bmatrix}$ | 0 | 0 |
| $\begin{Bmatrix} 5 & 1 & 7 \\ 2 & 2 & 2 \end{Bmatrix}$ | 0.6 | 0.4 |
| $\begin{Bmatrix} 7 & 1 & 5 \\ 2 & 2 & 2 \end{Bmatrix}$ | 0.9 | 0.7 |
| $\begin{Bmatrix} 5 & 5 & 5 \\ 2 & 2 & 2 \end{Bmatrix}$ | 0 | 0 |
| $\begin{Bmatrix} 7 & 5 & 1 \\ 2 & 2 & 2 \end{Bmatrix}$ | 1.1 | 1.1 |
| $\begin{Bmatrix} 5 & 3 & 7 \\ 2 & 2 & 2 \end{Bmatrix}$ | 0.7 | 0.6 |
| $\begin{Bmatrix} 7 & 3 & 5 \\ 2 & 2 & 2 \end{Bmatrix}$ | 0.4 | 0.3 |
| $\begin{Bmatrix} 7 & 5 & 3 \\ 2 & 2 & 2 \end{Bmatrix}$ | 1.1 | 0.9 |
| $\begin{Bmatrix} 7 & 1 & 7 \\ 2 & 2 & 2 \end{Bmatrix}$ | 0 | 0.2 |
| $\begin{Bmatrix} 5 & 5 & 7 \\ 2 & 2 & 2 \end{Bmatrix}$ | 0.4 | 0.2 |
| $\begin{Bmatrix} 7 & 5 & 5 \\ 2 & 2 & 2 \end{Bmatrix}$ | 1.1 | 0.7 |
| $\begin{Bmatrix} 7 & 7 & 1 \\ 2 & 2 & 2 \end{Bmatrix}$ | 0 | 0 |
| $\begin{Bmatrix} 7 & 3 & 7 \\ 2 & 2 & 2 \end{Bmatrix}$ | 0 | 0 |
| $\begin{Bmatrix} 7 & 7 & 3 \\ 2 & 2 & 2 \end{Bmatrix}$ | 0 | 0 |
| $\begin{Bmatrix} 7 & 5 & 7 \\ 2 & 2 & 2 \end{Bmatrix}$ | 0.5 | 0.4 |
| $\begin{Bmatrix} 7 & 7 & 5 \\ 2 & 2 & 2 \end{Bmatrix}$ | 0 | 0 |
| $\begin{Bmatrix} 7 & 7 & 7 \\ 2 & 2 & 2 \end{Bmatrix}$ | 0 | 0 |

Xuan, and Overhauser (CXO).¹⁵ CXO did not display $\omega_j(\mathbf{q})$ along the [111] direction because no data were available for comparison. We have calculated the spectrum along [111] by using the CXO fit (which describes the data for $[q00]$, $[qq0]$, $[00q]$, and $[q0q]$). Calculated $\omega_j(q)$ of the three (acoustic) modes for $[qqq]$ are shown in Fig. 4. Notice the very low frequencies of the shear modes at the zone boundary ($q=0.5$). There are no sharp dips, however, near $q=0.5$, so peaks in TDS would not be expected in an x-ray scan along [111]. This explains the absence of "satellites" in

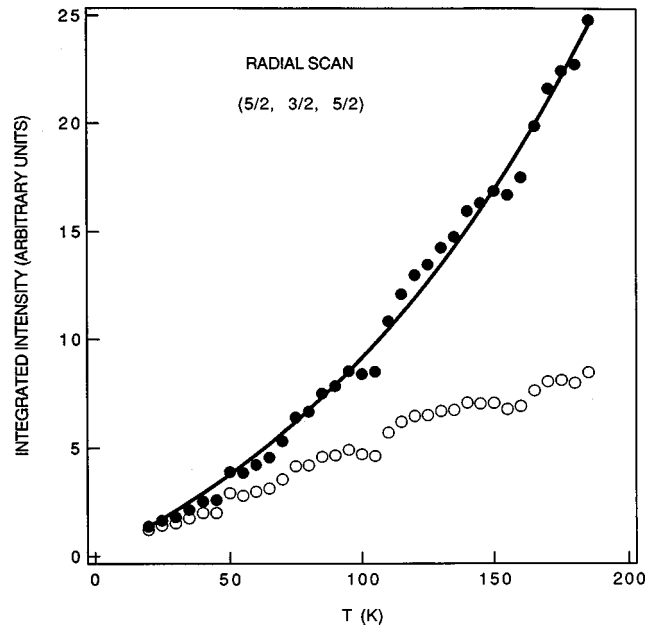


FIG. 3. Integrated intensity of the $(\frac{5}{2}, \frac{3}{2}, \frac{5}{2})$ "satellite" versus T . The open circles are the measured intensities; the solid points include a correction for the measured Debye-Waller factor. The curve is proportional to T/ω^2 , with $\omega(T) = \omega_0(1 - \gamma T)$ and $\gamma = 6.8 \times 10^{-4}$. (The In-crystal orientation was readjusted near 50, 110, and 170 K to compensate for thermal expansion.)

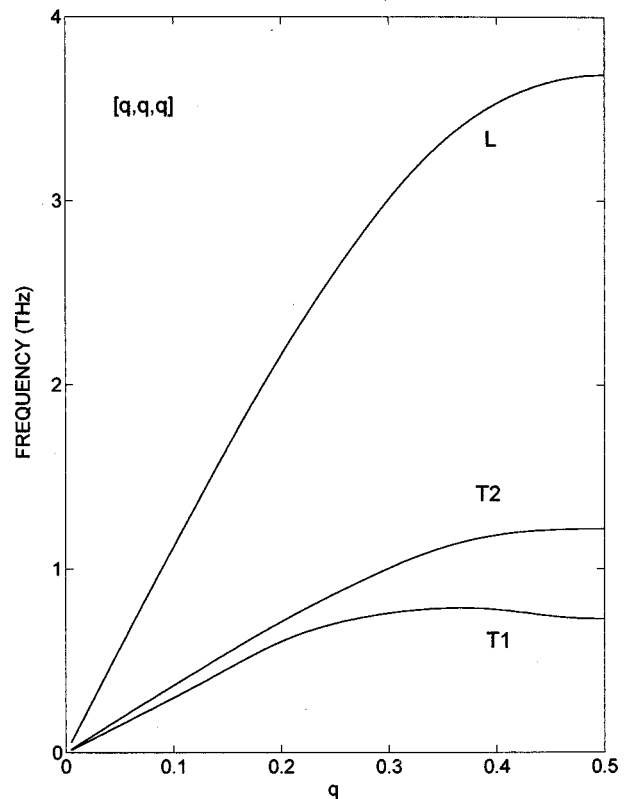


FIG. 4. Theoretical $\{\omega_j(\mathbf{q})\}$ for the phonon modes of In along the [111] direction. The dynamic pseudo-potential fit of Chen *et al.* (Ref. 15) to the experimental spectra along other directions was employed. (No data along [111] were available.)

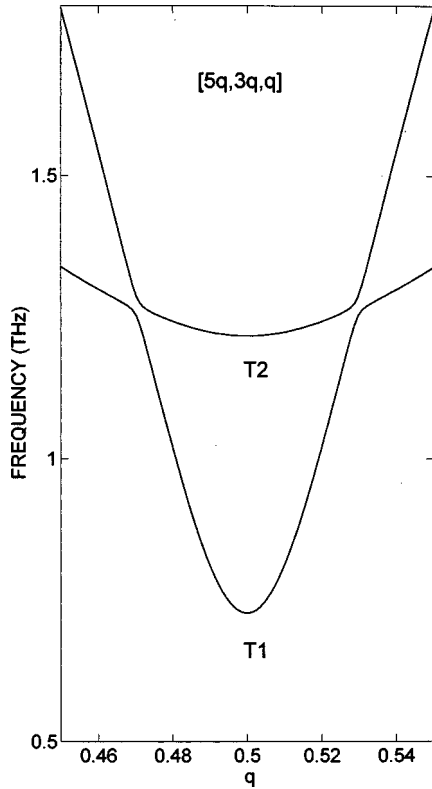


FIG. 5. Theoretical $\{\omega_j(\mathbf{q})\}$ for the two shear modes along a $[5q, 3q, q]$ trajectory. The sharp dip in the $T1$ mode near $q = \frac{1}{2}$ causes the TDS peaks. The mode crossings at $q = 0.47, 0.53$ should be noted.

Table I for the $(\frac{1}{2}, \frac{1}{2}, \frac{1}{2})$, $(\frac{3}{2}, \frac{3}{2}, \frac{3}{2})$, $(\frac{5}{2}, \frac{5}{2}, \frac{5}{2})$, and $(\frac{7}{2}, \frac{7}{2}, \frac{7}{2})$ families.

The cause of the TDS peak shown in Fig. 2 becomes clear by calculating $\omega_j(\mathbf{q})$ for $[5q, 3q, q]$. The frequencies of the two transverse modes are shown in Fig. 5. The sharp dip in ω for the $T1$ mode, centered at $q = 0.5$, causes the observed peak because TDS is proportional to ω^{-2} . TDS is also proportional to $(\hat{e}_j \cdot \hat{K})^2$, where \hat{e}_j is the polarization vector of the phonon and \hat{K} is the unit vector parallel to the x-ray scattering vector \mathbf{K} . Figure 6 shows that the polarization vectors do not rotate significantly in the scan interval of the TDS peak. (The interchange at the ends reflects only the crossing of the $T1$ and $T2$ modes.)

It must be remembered that $\omega_j(\mathbf{q})$ is periodic (in \mathbf{q}) with the periodicity of the reciprocal lattice. Accordingly, $\mathbf{q}_0 = (2.5, 1.5, 0.5)$, is the center of a hexagonal face of a unit cell, and $\{\omega_j(\mathbf{q}_0)\}$ equal the frequencies at $q = 0.5$ in Fig. 4. The q -space trajectory of the $[5q, 3q, q]$ scan forms a glancing angle of 17° with respect to the hexagonal face centered at \mathbf{q}_0 . We conclude that the peaks reported here arise from a sharp frequency dip of the slow shear mode ($T1$) along scans that form a glancing angle with a hexagonal zone boundary. The center of each hexagonal face is a saddle point for the $T1$ mode.

IV. THEORY OF THE TDS DIFFRACTION PEAKS

Since the Debye temperature of In is 108 K, the high-temperature expression¹⁶ for the x-ray scattering intensity $I(\mathbf{K})$ caused by emission or absorption of a phonon may be used at room temperature

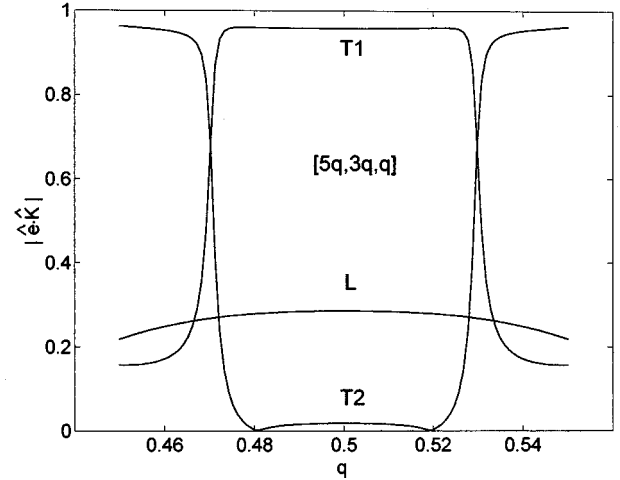


FIG. 6. Behavior of the polarization vectors $\hat{e}_j \cdot \hat{K}$, relative to the x-ray scattering unit vector \hat{K} along a $[5q, 3q, q]$ trajectory. The sharp variations near $q = 0.47, 0.53$ are associated with the crossings of the $T1$ and $T2$ modes, shown in Fig. 4.

$$I(\mathbf{K}) = \frac{Nk_B T}{M} |f(K)|^2 e^{-2W} \sum_{j=1}^3 \frac{|\hat{e}_j \cdot \mathbf{K}|^2}{\omega_j^2}. \quad (4)$$

M is the atomic mass, N is the number of atoms in the diffraction volume, $f(K)$ is the x-ray form factor for scattering vector \mathbf{K} ,¹⁷ and $\omega_j(\mathbf{q})$ is the phonon frequency for wave vector \mathbf{q} and polarization \hat{e}_j . (The sum is over the three acoustic modes of In.) The exponent in the Debye-Waller factor is

$$2W(\mathbf{K}) = \frac{k_B T}{NM} \sum_{\mathbf{q}} \frac{1}{\omega_j^2(\mathbf{q})} |\hat{e}_j(\mathbf{q}) \cdot \mathbf{K}|^2. \quad (5)$$

\mathbf{q} is summed over the N wave vectors of the Brillouin zone and $\mathbf{K} = \mathbf{G} \pm \mathbf{q}$, where \mathbf{G} is a reciprocal lattice vector. The Debye-Waller factor was measured by studying the T dependence of four Bragg reflections. We found

$$2W = 10.5 \left(\frac{\sin \theta}{\lambda} \right)^2. \quad (6)$$

λ is here, the x-ray wavelength in Angstroms and

$$\frac{\sin \theta}{\lambda} = \frac{1}{2a} \left[k_x^2 + k_y^2 + k_z^2 \left(\frac{a}{c} \right)^2 \right]^{1/2}, \quad (7)$$

where \mathbf{k} is the scattering vector \mathbf{K} , but in (dimensionless) reciprocal lattice units, and a is in \AA . Finally, the Lorentz-polarization factor L of Eq. (4) is

$$L = \frac{1 + \cos^2(2\theta)}{2 \sin(2\theta)}. \quad (8)$$

(This factor is appropriate for calculating the integrated intensities that are to be compared with those measured with the CAD4 diffractometer.) The computed TDS scattering for $[5, 3, 1]$ and $[3, 1, 1]$ trajectories are shown in Figs. 7 and 8 together with the corresponding data. The agreement is satisfactory. The vertical heights of both curves were adjusted for optimum fit, but no attempt was made to include absorp-

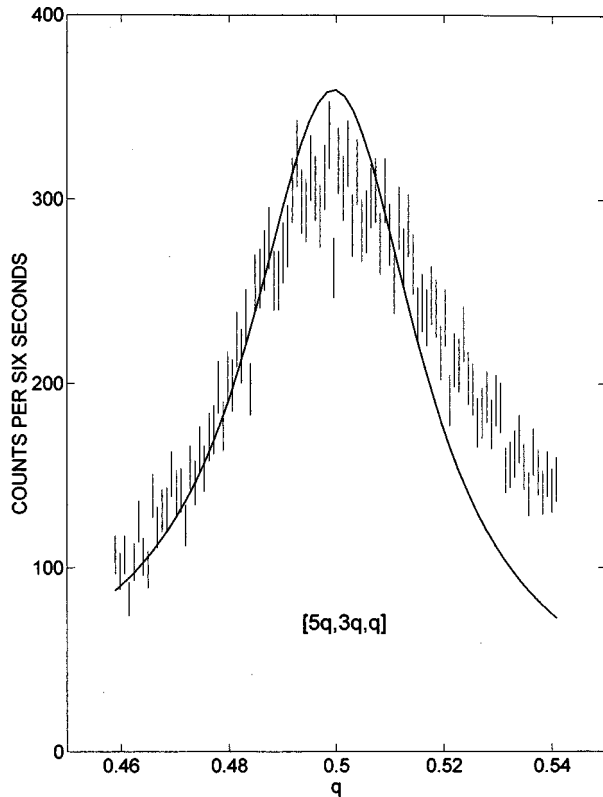


FIG. 7. The TDS peak along $[5q, 3q, q]$. The theoretical curve shown was computed from Eq. (4) and scaled along the vertical axis for an optimum fit. The glancing angle of the trajectory relative to the hexagonal face it pierces is approximately 17° .

tion corrections in the theory (which could modify slightly the skew asymmetry of the calculated peaks).

Another challenging test of the theory is to compute the integrated intensities for all 40 half-integral families listed in Table I and to compare them with the observed room-temperature intensities listed in column 1. The scan width of θ was 5° (for each family) and each scan comprised 96 points. The “raw” integrated intensity was defined as the sum of the 96 counts minus the background, which was taken to be 96 times the average of the first 16 and last 16 points. In order to minimize effects of absorption the strongest peak of each family was chosen. The “raw” intensities were then normalized so that the $(\frac{5}{2}, \frac{3}{2}, \frac{1}{2})$ family had unit intensity.

The TDS scattering was then calculated for the same 96 points of each experimental scan; and the theoretical intensity was defined by the same scheme just described. The theoretical relative intensities are listed in column 2. The remarkable agreement allows one to conclude that the ob-

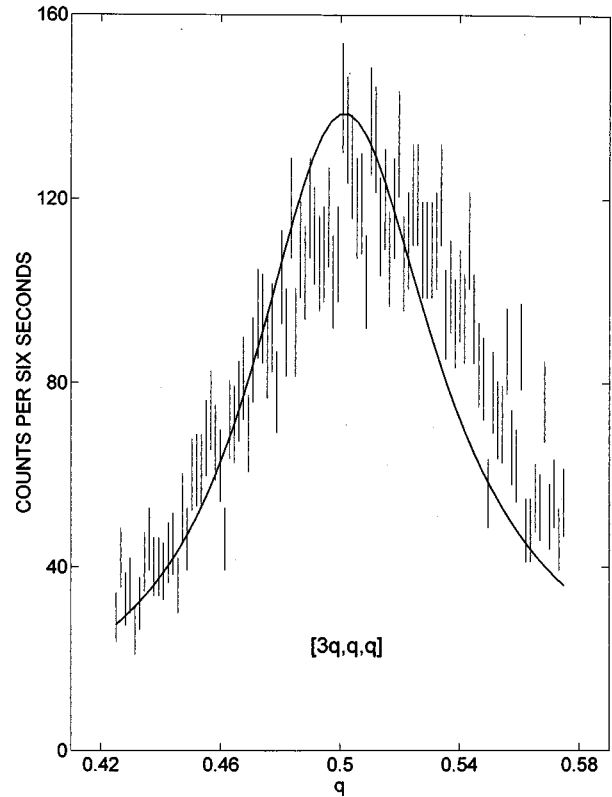


FIG. 8. The TDS peak along $[3q, q, q]$. The theoretical curve shown was computed from Eq. (4) and scaled along the vertical axis for an optimum fit. The glancing angle of the trajectory relative to the hexagonal face it pierces is approximately 10° .

served half-integral “satellites” arise from TDS by the slow-shear mode (T_1) near the $(\pm\frac{1}{2}, \pm\frac{1}{2}, \pm\frac{1}{2})$ points of the Brillouin-zone boundary.

Appearance of TDS peaks is a consequence of the sharp dip in $\omega_1(\mathbf{q})$ along trajectories that are nearly parallel to the hexagonal faces of the Brillouin zone boundary. This behavior is predicted successfully by the dynamic pseudopotential model^{14,15} for phonons in In, since there is no experimental data for $\{\omega_j(\mathbf{q})\}$ near $(\frac{1}{2}, \frac{1}{2}, \frac{1}{2})$.

The puzzles that prompted this research—the behavior of $c(T)$, Fig. 1, and the 10% reduction in the T^3 specific heat on entering the superconducting state^{3,4}—remain unsolved.

ACKNOWLEDGMENTS

We are grateful to S. N. Ehrlich for his kind assistance at beamline X-18A of the National Synchrotron Light Source. We also acknowledge support from the Division of Materials Research, National Science Foundation.

¹J. Graham, A. Moore, and G. V. Raynor, *J. Inst. Met.* **84**, 86 (1955); see also, N. Mediah and G. M. Graham, *Can. J. Phys.* **42**, 221 (1964).

²G. A. Alers and D. L. Waldorf, *IBM J. Res. Dev.* **6**, 89 (1962).

³C. A. Bryant and P. H. Keesom, *Phys. Rev.* **123**, 491 (1961).

⁴H. R. O’Neal, N. M. Senozan, and N. E. Phillips, in *Proceedings of the Eighth International Conference on Low-Temperature Physics, 1962*, edited by R. O. Davies (Butterworths, Washington, 1963), p. 403.

⁵A. W. Overhauser, *Phys. Rev.* **167**, 691 (1968).

⁶A. W. Overhauser, *Phys. Rev.* **128**, 1437 (1962).

⁷Bernhard Mühlshlegel, *Z. Phys.* **155**, 322 (1959).

⁸A. W. Overhauser, *Phys. Rev. B* **3**, 3173 (1971).

⁹Y. R. Wang and A. W. Overhauser, *Phys. Rev. B* **32**, 7103 (1985).

¹⁰M. Danino and A. W. Overhauser, *Phys. Rev. B* **26**, 1569 (1982).

¹¹R. R. Hewitt and W. D. Knight, *Phys. Rev. Lett.* **3**, 18 (1959).

¹²W. W. Simmons and C. P. Slichter, *Phys. Rev.* **121**, 1580 (1961).

- ¹³H. G. Smith and W. Reichardt, *Numerical Data and Functional Relationships in Science and Technology*, edited by K.-H. Hellwege and J. L. Olson, Landolt-Börnstein, New Series, Group III, Vol. 13, pt. a (Springer-Verlag, Berlin, 1981), p. 67.
- ¹⁴Y. R. Wang and A. W. Overhauser, Phys. Rev. B **35**, 497 (1987).
- ¹⁵X. M. Chen, Yashu Xuan, and A. W. Overhauser, Phys. Rev. B **43**, 1799 (1991).
- ¹⁶P. Bruesch, *Phonons: Theory and Experiment, II* (Springer-Verlag, Berlin, 1986).
- ¹⁷*International Tables for X-ray Crystallography, IV* (Kynoch, Birmingham, 1974).